

# The Sixth Sense with Artificial Intelligence

An Innovative Solution for Real-Time Retrieval of the Human Figure Behind Visual Obstruction

Kevin Meng, ACM Student Member  
Plano West Senior High School  
Plano, Texas  
kevin.meng.01@gmail.com

Yu Meng, Ph.D., IEEE Senior Member  
Oncor Electric Delivery  
Dallas, Texas  
yu.meng@oncor.com

**Abstract**—Overcoming the visual barrier and developing “see-through vision” has been one of mankind’s long-standing dreams. However, visible light cannot travel through opaque obstructions (e.g. walls). Unlike visible light, though, Radio Frequency (RF) signals penetrate many common building objects and reflect highly off humans. This project creates a breakthrough artificial intelligence methodology by which the skeletal structure of a human can be reconstructed with RF even through visual occlusion. In a novel procedural flow, video and RF data are first collected simultaneously using a co-located setup containing an RGB camera and RF antenna array transceiver. Next, the RGB video is processed with a Part Affinity Field computer-vision model to generate ground truth label locations for each keypoint in the human skeleton. Then, a collective deep-learning model consisting of a Residual Convolutional Neural Network, Region Proposal Network, and Recurrent Neural Network 1) extracts spatial features from RF images, 2) detects and crops out all people present in the scene, and 3) aggregates information over dozens of time-steps to piece together the various limbs that reflect signals back to the receiver at different times. A simulator is created to demonstrate the system. This project has impactful applications in medicine, military, search & rescue, and robotics. Especially during a fire emergency, neither visible light nor infrared thermal imaging can penetrate smoke or fire, but RF can. With over 1 million fires reported in the US per year, this technology could save thousands of lives and tens-of-thousands of injuries.

**Keywords**—radio frequency, FMCW, radar, computer vision, CNN, LSTM, RPN, pose, reconstruction, many-to-many imaging

## I. INTRODUCTION

As humans, our ability to perceive information about our environment suffers from a significant bottleneck from the physical properties of visible light: it is either reflected or absorbed by objects in our immediate surroundings, allowing various items such as furniture and walls obstruct our view of entities we want to see. Especially in the scenarios of search & rescue, non-invasive healthcare, and military operations, the ability to perceive human presence and recover the figure on detected bodies could provide a remarkable improvement to these systems’ functionalities.

However, most other types of radiation on the electromagnetic spectrum are either too powerful, to the extent of causing adverse health effects by exposure, or too high in wavelength, causing them to pass straight through objects and not reflect to the necessary degree. In contrast, Radio Frequency (RF) electromagnetic radiation is safe, can traverse materials of low reflective index such as walls and furniture, and reflect off humans. This makes them an ideal choice for creating a system

that can extend human vision to transcend the physical limits of traditional vision.

There are many applications for the solution proposed in this paper, one of which is Search & Rescue: RF can detect victims behind an assortment of obstructions. 1.35 million died and 218 million people were injured in 6,873 natural disasters worldwide between 1994 and 2013. [1] An especially killer application of this technology is that RF figure imaging can resolve a dire problem that there is presently no solution to. In a fire, no technological instruments can help us detect life from safety; neither visible light cameras nor thermal imaging can traverse visual and IR pollution from smoke and fire. RF imaging can provide not only detection but also figure retrieval. [11]

## II. PROJECT GOAL

This paper aims to establish an innovative methodology that allows people to detect the human figure through visual obstruction. This will allow for a multitude of impactful applications, as outlined in §I.

Figure 1 functions as a sketch of the intended design. RF signals will be transmitted and received by an RF imaging device. While some signals will be reflected, absorbed, or attenuated by the intermediate obstruction, most signals will penetrate and reflect off the human. Using a computing device, raw data is extracted and preprocessed, then inputted into an artificial intelligence module, which extracts the pose.

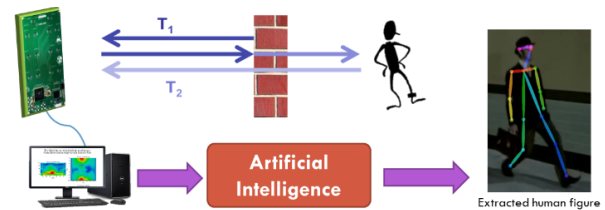


Figure 1. Diagram of intended design

## III. RELATED WORKS

### A. Figure Retrieval Using Physical Sensors

Estimation of the human figure via physical sensors has been developed extensively and put into commercial production [37], partially due to the relative ease with which the data may be extracted using inertial measurement units [38] that consist of accelerometers and gyroscopes. However, these solutions require the target user to wear a bevy of cumbersome sensors on their bodies. In some cases, including search & rescue cases or

military operation, this bottleneck defeats the purpose of trying to estimate the human figure. In other cases, this causes a major inconvenience for users, as in medical healthcare.

### B. Figure Retrieval Using the RGB Domain

Analyzing the human figure using RGB video has also been a hotspot of recent computer vision research, as the high spatial resolution of color images allows for an accurate and complete extraction of the human pose. Notably, Zhe Cao et al. [20] have developed a state-of-the-art pose estimation technique using Part Affinity Fields to extract 2D poses from images, following a bottom-up approach, in which all keypoints in the image are first mapped out and then subsequently joined together into groups.

### C. Figure Retrieval Using the RF Domain

In the past, Radio-Frequency (RF) signals (3kHz – 300kHz) were used sparingly in human localization problems, because they required the user to carry a Wi-Fi or Cellular-enabled device to query the person’s location [39, 40]. This provided little advantage relative to the solutions mentioned in §III-A. Recently, however, researchers have begun studying the usage of RF signal reflections off human bodies to gather information on human figures. These works can be stratified into two primary categories. First is the research concerning high-precision imaging using 100GHz frequencies (colloquially known as mmWave). This provides precise detail but is incapable of penetrating walls or furniture. In contrast, the second category of work concerns penetrative applications using Wi-Fi-band signals ( $3\text{GHz} \leq f \leq 10\text{GHz}$ ). These EM waves provide less detail but allow the penetration of common building materials. Discussions will focus on the second type of research.

Currently, few RF tracking systems can provide specific detail; most works achieve coarse approximation of the human figure, including localizing the general location of a body [41], monitoring a person’s walking speed [42], and tracking arm motion to characterize its motion [43]. In 2018, Mingmin Zhao et al. [35] proposed a deep learning system in CVPR that could identify human keypoints from RF signal power reflection heatmaps. This work aims to build upon Zhao et al.’s research in improving pose performance. Contributions are noted in §XII.

## IV. MATERIALS AND TECHNOLOGIES

Programming and scripting languages used include Python 3.6, Visual C++ v. 141, GNU C++11 (GCC 6.4.0), and Bash. Integrated Development Environments JetBrains PyCharm, Visual Studio Community 2017, Visual Studio Code, ConEmu Console Emulator, and MobaXTerm SSH Tool were used to develop necessary software. Networks are implemented in the TensorFlow deep learning framework, along with Python scientific data processing packages Numpy, Scipy, and Scikit-learn. Matplotlib and pygame were used to visualize necessary elements. Neural networks were trained on a Nvidia GeForce GTX 1080Ti GPU Server. Radio-Frequency data was collected using a commercially-available Walabot RF Antenna Array and processed using its accompanying SDK. An RGB web-camera was used for color video collection. The demonstration was created with Adobe Premiere Pro CC and Wondershare Filmora. The state-of-the-art OpenPose CV Gait Analysis tool was employed to extract poses.

## V. PROCEDURAL FLOW

This project proposes a system in which antenna array RF signals are computationally analyzed by a deep learning model to infer the pose of person(s) though visual obstruction, including walls and furniture. In this manner, a critical bottleneck of visible light-based vision is relieved, allowing people to transcend the physical boundaries imposed on sight by visible light. The justification behind the usage of deep learning is outlined in §IX.

An analysis of the scientific problem yields key observations for the formulation of the 5-component project flow depicted in Figure 2. The following sections will explain details important to understanding the procedural flow and model design choices.

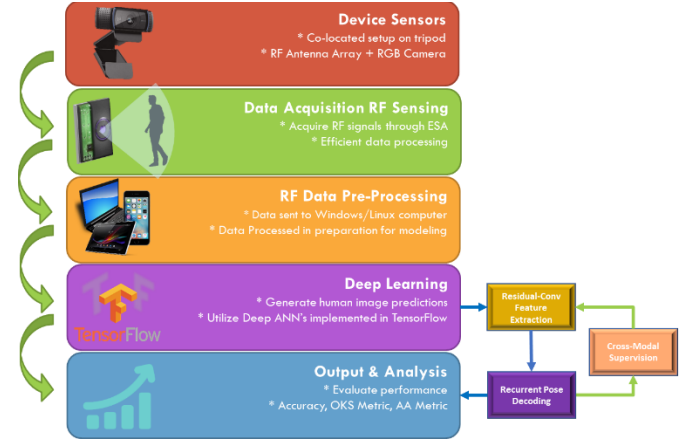


Figure 2. 7-Component Project Flow Diagram

## VI. DEVICE SENSORS

Sensory data is collected simultaneously in two separate respects: RF reflection signals and RGB images (Figure 3). The RF signals will be used as input to the deep learning model during training and inference, while the RGB images will be inputted to a second computer vision model during training to cross-modally supervise the RF image-to-pose model. To ensure that images from both the camera and webcam are representative of the same viewing angle, the FMCW antenna array and RGB camera are mounted in positions fixed relative to each other on a tripod. Furthermore, to ensure synchronization in the time domain, the two inputs are synced with the Network Time Protocol to within ~5ms of error between RF and RGB measurements. Justifications for using both RF and RGB sensors is detailed in §IX-B.

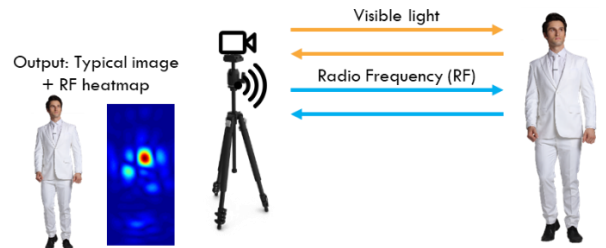


Figure 3. Visual Depiction of Camera Setup

### A. FMCW Radio-Frequency Antenna Array

The RF imaging device used in this project is an antenna array [2] – a proven, reliable method of transmitting signals into the environment and receiving back the reflections. Hardware 2D array of antennas capable of transmitting and receiving RF signals

Table 1. Technical Specifications

RADAR Type	Frequency Modulated Continuous Wave RADAR
Model	Walabot Pro
Number of Antennas	18
External Power supply	5V
Current Consumption	0.4-0.9 A
Average Transmitted Power	-41dBm/MHz
Frequency Range	3.3-10 GHz
Software API	C#/VB/C++/ python
Communication Protocol	USB2.0 480 Mbit
Measurement Distance	0 to 10 meter
Operating System	Windows / Linux

The array transmits RF signals in full compliance with FCC regulation. The chosen parameters are: frequency  $f$  bandwidth from 3.3GHz to 10GHz and 2) transmit power  $p = -41dBm \approx 100pW$  (1/1000 power of Wi-Fi). It is capable of imaging on the Spherical coordinate system  $(\theta, \phi, r)$ .

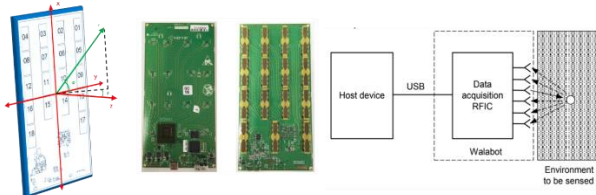


Figure 4. Radio-Frequency Antenna Array

### B. RGB Camcorder

The Logitech HD Pro Webcam C920 is used to capture full-color RGB video of the environment. It features widescreen video recording at 1080p resolution and supports connection to computers via the USB-A protocol. Windows, Linux, and Mac are all supported. The camera resolution is downgraded to 640 by 480 to preserve sufficient information while preventing overflow of storage space.

### C. Co-Located Setup with Array and Camera

The Camera and Array are spatially co-located to ensure that the outputs are consistent. Figure 5 shows the mounting location of the two devices on the tripod, while table 2 details the data collection from the various sensory inputs.



Figure 5. Camera and Array Setup

Table 2. Sensory Input, Data Acquisition, and Data Format

Sensors	Data Acquisition	Data Format
FMCW Antenna Array	RF reflections from environment	.csv file
RGB Camera	RGB image of human(s) in environment	.mp4 file

## VII. PARAMETER SELECTION & DATA ACQUISITION

### A. Through-Obstruction Imaging Technique

In this project, a primary challenge lies in determining a novel method to transcend the boundaries imposed on vision by the  $\sim 380nm$  to  $\sim 750nm$  wavelength range of the electromagnetic spectrum, better known as visible light. At this wavelength, it fails to penetrate any kind of opaque object. This becomes a critical issue in military or search and rescue situations, for example, as lives hinge upon being able to detect human life without line-of-sight.

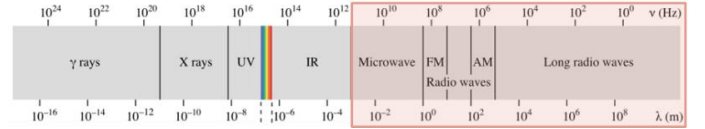


Figure 6. Comparison of Different Waves

Alternatively, radio frequency (RF) waves, just like our Wi-Fi signals, can penetrate walls. In addition, humans have high reflective coefficients [3]; therefore, RF waves can be used to break the barrier. To harness these types of EM waves, this project employs antenna arrays.

The following subsections will detail the implementation and key operative features of these imaging devices.

### B. Single Transmitter and Receiver Antenna Pair

An RF signal is a waveform which has a periodically phase factor. By calling or sampling the received signal, both amplitude and its phase can be recorded. The sampled signal can be represented as a complex discrete function of time  $t$  as

$$s_t = A_t e^{-j2\pi \frac{r}{\lambda} t} \quad (1)$$

where  $r$  is the distance traveled by the signal,  $\lambda$  is its wavelength, and  $A$  is its amplitude. [4]

The antennas have broadband performance covering the 3-10GHz frequency range. Measured gain patterns at 4 GHz, 6 GHz and 8 GHz are shown in Figure 7. Note that, at certain angles, the gain of each antenna falls to zero; this indicates a dead-zone. [5] To overcome this physical limitation, a full array of transceiver antennas is used.

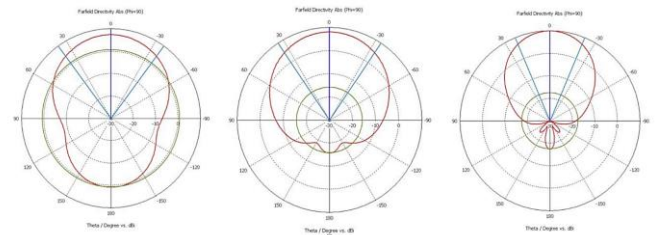


Figure 7. Gain Patterns & Receptivity at Different Frequencies

### C. Antenna Array

Antenna arrays can be used to identify the spatial direction from which an RF signal arrives with significantly improved performance compared to a single antenna. They also solve the issue of antenna dead zones, as mentioned in the previous subsection.

The power emanating from a certain angle  $\theta$  can be computed as:

$$P(\theta) = \left| \sum_{n=1}^N s_n e^{j2\pi \frac{nd \cos \theta}{\lambda}} \right| \quad (2)$$

where  $s_n$  is signal received at antenna  $n$ ,  $d$  is distance between adjacent antennas, and  $\lambda$  is the RF signal wavelength. [6]

$$\Delta\theta = 0.886 \frac{\lambda}{nd} \quad (3)$$

where  $n$  is number of transmitters, and  $d$  is the space interval between adjacent antennas. [7] If one dimension is considered,  $nd$  is the physical size of the RF antenna array. Overall, the advantage of this setting is to sharpen the image.

### D. Frequency-Modulated Continuous Wave (FMCW)

Although antenna arrays, by themselves, are able to perceive spatial location, they are not sensitive to depth. A straightforward method of measuring depth is using the distance formula:  $d = ct$ , where  $c$  is the speed of light. However, the time of flight  $t$  is extremely difficult to measure, as it is typically in the nanosecond range. [8]

FMCW is a special radar technique that allows the measurement of reflector depth in a feasible manner. Rather than attempting to capture the nanosecond difference between time of transmission and receipt, it sends a signal linearly modulated in frequency w.r.t. time (Figure 9).

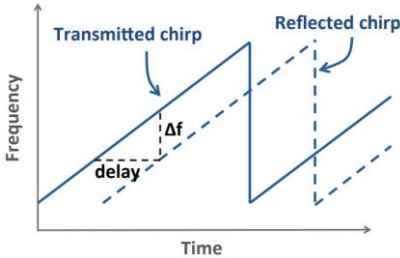


Figure 9. FMCW Linear Frequency Modulation

In this manner, rather than measuring the time delay between the transmitted chirp and reflected chirp, the  $\Delta f$  is measured; this can be accomplished using a low-cost, passive hardware device called a mixer. [9] To compute  $\Delta t$  given  $\Delta f$ , we simply use the modulation slope  $k$ :

$$\Delta t = \frac{\Delta f}{k} \quad (4)$$

Equipped with this knowledge, we can compute the reflected power emanating from a depth  $r$  using eq. 5:

$$P(r) = \left| \sum_{t=1}^T s_t e^{j2\pi \frac{kr}{c} t} \right| \quad (5)$$

where  $k$  is the slope of the frequency vs. time line and  $c$  is the speed of light. [10] Furthermore, depth resolution depends on the bandwidth of the frequency chirps, as shown in the equation below:

$$\Delta r = \frac{c}{2B} \quad (6)$$

where  $B$  is the difference between the maximum and minimum frequencies of the chirps. [11] In summary, FMCW increases depth resolution.

### E. Antenna Array SDK API for Project Implementation

Following the hardware considerations, we now examine the interface with the software. The Walabot API, contained in Walabot Developer Pack SDK [12], is used to interface with RF antenna array hardware. Data is transposed into a 3D matrix representing reflected signal power, and  $R(\theta, \phi, r)$  is used to query the raw reflected signal power from each voxel in 3D space.

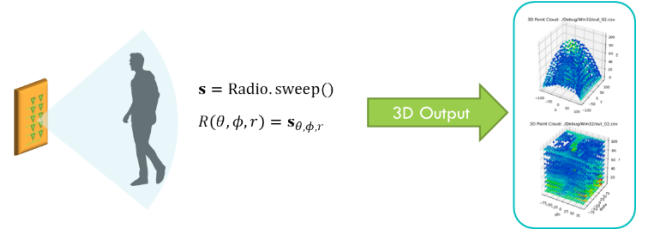


Figure 10. Collection Setup

### F. Data Acquisition Output Format

Table 3. RF and RGB Sensors

Sensors	Data Acquisition	Data Format
FMCW Antenna Array	RF reflections from environment	.csv file
RGB Camera	RGB image of human(s) in environment	.mp4 file

## VIII. RF DATA PRE-PROCESSING

### A. Coordinate Conversion

Sensor data in Spherical coordinates is retrieved using Walabot Developer SDK API calls. However, Cartesian representation is desired to represent 3D space [13]:

$$\begin{cases} x = r * \sin \theta \\ y = r * \cos \theta * \sin \phi \\ z = r * \cos \theta * \cos \phi \end{cases} \quad (7)$$

As such, eq. 7 is used to convert between the two coordinate systems.

### B. Dimensionality Reduction

A 3D Point Cloud is computationally expensive to compute over. To reduce dimensionality, it can be simplified into two 2D heatmaps, vertical and horizontal.



$$\begin{cases} R_{horz}(\theta, r) = \sum_{\phi=\phi_{min}}^{\phi_{max}} R(\theta, \phi, r) \\ R_{vert}(\theta, \phi) = \sum_{r=r_{min}}^{r_{max}} R(\theta, \phi, r) \end{cases} \quad (8)$$

$$\begin{cases} R_{horz}(x, z) = \sum_{y=y_{min}}^{y_{max}} R(x, y, z) \\ R_{vert}(x, y) = \sum_{z=z_{min}}^{z_{max}} R(x, y, z) \end{cases} \quad (9)$$

Equations 8 and 9 are used to sum all the values on two planes to reduce the 3D data into two 2D representations that still retain the 3D context.

### IX. PHYSICS-DRIVEN DESIGN CONSIDERATIONS

In §VIII, the final step of RF data processing is performed. From this, both horizontal and vertical heatmaps are outputted to represent the person in the RF domain. However, analysis of these heatmaps, especially the vertical one, reveal a challenge.

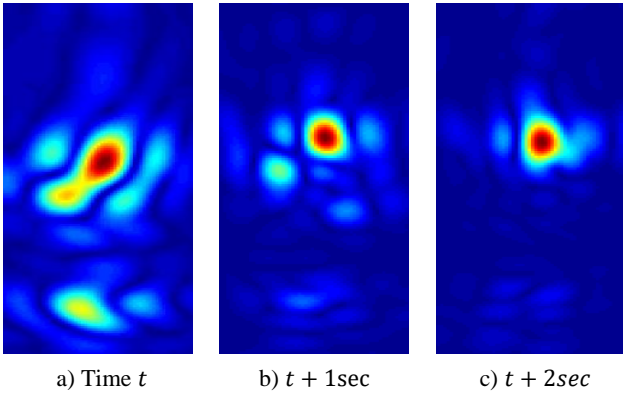


Figure 12. Three Vertical Heatmaps Captured in 1sec Succession [7]

As seen in Figure 12, not all body parts show up on a single RF heatmap. Figure 12(a) shows many limbs, but 12(b) and 12(c) show only parts of the body, many of which show very low reflection power. It is only through all 3 images that we can roughly approximate where each limb is at each point in time.

This section aims to A) identify the physical cause of this phenomenon and B) outline a solution that employs state-of-the-art artificial intelligence while addressing several technical challenges that the utilization of AI entails.

#### A. Reflection and Scattering

Reflection occurs when a beam impinges upon a surface smooth relative to its wavelength; the physical behavior of the wave will obey the Law of Reflection, that  $\theta_{incident} = \theta_{reflected}$ . [14] On the other hand, scattering occurs when a wave impinges upon an object that is rough or uneven relative to the signal's wavelength, causing the reflected energy to spread out or "scatter" in many directions. [15] Figure 13 depicts this phenomenon.

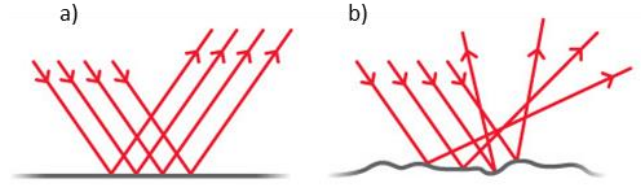


Figure 13. Contrast Between Reflection and Scattering

In experimental settings, the  $\lambda$  of RF is  $\sim 5\text{cm}$ , as opposed to the nanometer-range wavelength of visible light. Therefore, the physics of RF imaging are fundamentally different from that of optical (visible light) imaging. With respect to the miniscule wavelength of visible light, surfaces are rough and therefore function as scatterers, as seen in Figure 13(b). However, in the  $\sim 5\text{cm}$  wavelength of RF, objects function as reflectors. Figure 14 demonstrates this by showing that: (a) Only signals that fall along the normal to the surface are reflected off toward the device, (b) the human body has a complex surface, but at any point in time only signals close to the normal to the surface are reflected toward the device, and (c) As the person walks, different body parts reflect signals toward the device and become visible to the device.

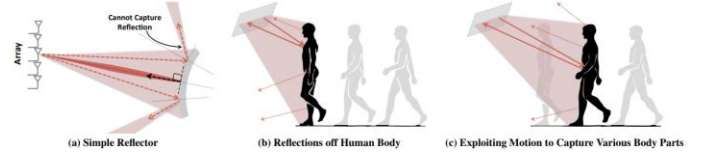


Figure 14. Example of the Effect of RF Specularity [7]

#### B. Artificial Intelligence-Based Solution Sketch

Based on observations made in the previous subsection, we deduce that RF imaging, unlike optical imaging, is not a one-to-one scenario. In optical imaging, one sampling of a group of lens-focused light waves is sufficient to reconstruct a full image – this is because objects scatter light waves. However, using RF imaging, not all critical limbs show up at once. Therefore, we must consider not just the current RF image, but also all that come before it in order to piece together the various limbs that reflect signals back to the receiver at various times.

A computational method by which this can be accomplished is deep learning. Namely, Recurrent Neural Networks (RNN) [16] have been the workhorses behind recent breakthrough applications in analyzing sequential data, because they consider information all the way from time  $\max(0, t - K)$  to  $t$ , where  $K$  is the researcher-specified depth of backpropagation. In this manner, RNN's are capable of accumulating information over time to make an accurate pose inference. RNN's can also be combined with Convolutional Neural Networks (CNN) [17], which learn spatial features from RF heatmaps. In tandem, CNN's and RNN's jointly learn spatio-temporal patterns.

#### C. Cross-Modal Supervision Using RGB Color Camera

We now reach an issue: in this supervised machine learning task, ground-truth labels are necessary. However, it is infeasible to manually generate these supervisory labels (consider each sample containing  $4 \text{ sec} \times 10 \text{ Hz} \times 15 \text{ keypoints/frame/sample} = 600 \text{ keypoints/sample}$ ). Therefore, we must provide some sort of ground-truth label for the deep learning

model to learn from. To address this challenge, an RGB color camera is introduced to help teach the deep learning model – this is the camera mentioned in §VI. RF and RGB images acquired by the sensors describe the same person at the same moment in time, just in different domains. The cross-modal supervision algorithm is detailed in §X-B.

#### D. Initial Naïve Solution

Now, we both have the ground-truth human figure (typical image) we are trying to reconstruct and the RF heatmap that we are attempting to learn from (RF heatmaps). Naively, we may consider trying to recover the full-color RGB rendition of the person behind the wall (Figure 15). Therefore, we may attempt to explicitly transfer between the RF image domain and the RGB image domain [reference domain transfer works], as shown in Figure 16(a), using a model such as a Generative Adversarial Network (GAN) [18] or Variational Autoencoder (VAE) [19].

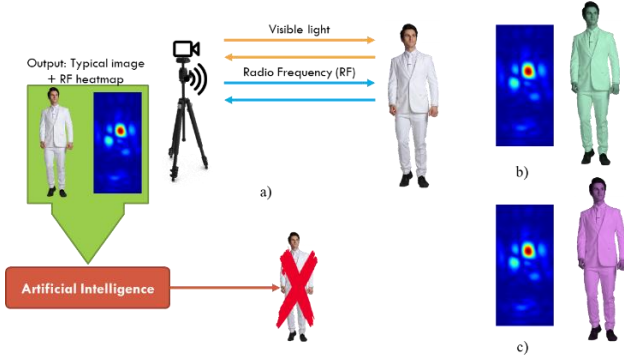


Figure 16. RF-to-RGB Conversion Diagram

However, there are several issues with this methodology. Particularly, note Figure 16(b) & (c). The pixels in an RGB are significantly affected by the choice of clothing that a person wears; however, the RF signatures are identical. This creates a problem: if 1 RF signature can map to multiple RGB signatures, how can we reliably tell what a person's full-color image will be, solely using RF? Moreover, the style of hair, height, gender, and skin color of a person can change without significantly impacting the received RF output.

The deep learning model that would be produced using this solution approach risks over-fitting or simply a lack of ability to converge. A more realistic solution is desired.

#### E. Refined Solution

Rather than attempting to recover the full-color and full-resolution image, we desire a solution whose output still retains the necessary information to deduce a pose from RF heatmaps but does not demand as much extraneous detail as the solution in subsection D.

To accomplish this, the RGB image is simplified down from thousands of pixels into just 15 specific keypoints (BODY\_15) that delineate where all the points of interest are. Using an openly-available computer vision gait analysis tool named OpenPose [20], all points are extracted. Ultimately, these points constitute the ground truth for the AI model to train on. The specific definition of BODY\_15 can be found in §X-A.

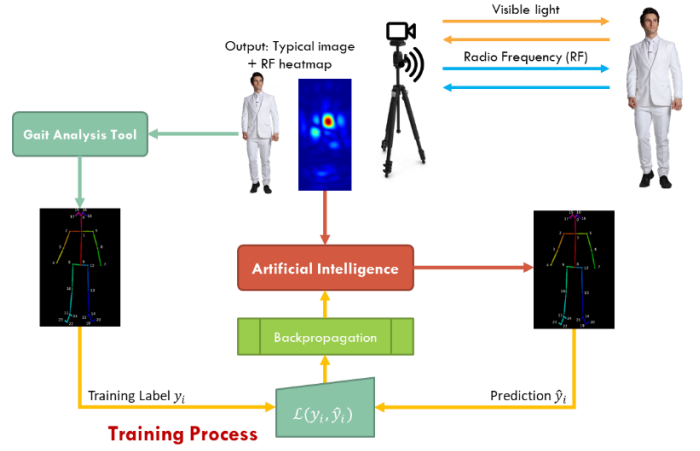


Figure 17. RF-to-RGB Training Diagram

In summary, as depicted in Figure 17, we finally reach a feasible methodology to train an artificial intelligence module to transform RF heatmaps to a pose that represents the person's figure – even through visual obstruction. In the training process, an RGB camera is used to assist the training of the AI model by providing the ground-truth pose locations. Then, during the prediction, or inference, stage, the AI model has been trained to deduce human pose solely from RF heatmaps; therefore, we do not need the RGB camera at that stage.

Once the training process is complete, the model's learned parameters are fixed. The model can now reconstruct the human pose, even through walls (Figure 32), using RF information. During the prediction/inference, the RGB camera is removed, as it was used solely to teach the deep learning model how to map RF data to a reconstructed pose. The final inference setup is shown below in Figure 32.

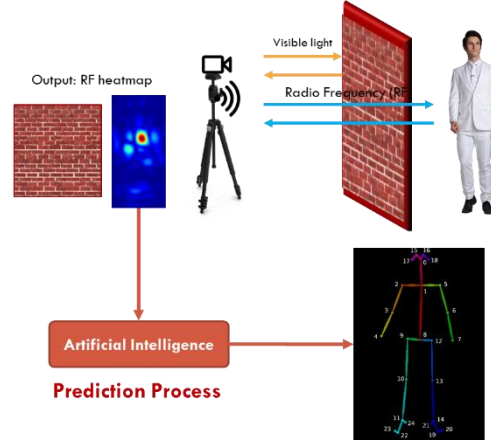


Figure 32. RF-to-RGB Prediction Diagram

## X. ARTIFICIAL INTELLIGENCE ARCHITECTURE & ALGORITHMS

### A. Body Pose Keypoint Definitions

Figure 18 depicts the BODY\_15 definition of the 15 body keypoints that are to be detected through visual obstruction in this project. These include: head, shoulder, elbow, hand, hip, knee, and foot datapoints.

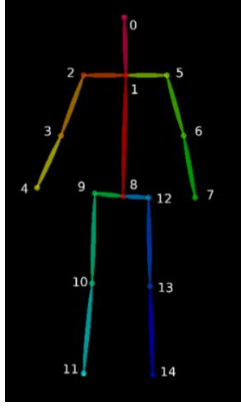


Figure 18. BODY\_25 body keypoint definitions

At each timestep, each of these keypoints will be classified into a pixel on the screen. Note that only indices 0 through 14 are used for classification; the specularity and low spatial resolution of radio-frequency image data is non-conducive to detecting such granular points.

### B. Overview of Cross-Modal Supervision Algorithm

Because it is infeasible to manually label radio-frequency image with the appropriate keypoints, a more efficient manner of generating supervisory labels is desired. This involves a computational method utilizing a deep learning model cross-modally dependent on another.

Let  $\mathcal{M}_1$  denote an initially untrained deep learning model that takes radio-frequency heatmap images as input and outputs 15 bodily keypoints at each time step. Let  $\mathcal{M}_2$  denote a pre-trained deep learning model that takes RGB images as input and outputs 15 body keypoints at each time step.

$\mathcal{M}_1$  will be cross-modally supervised by  $\mathcal{M}_2$  during training. More concretely, each training sample consists of only an input  $x_i$ , which contains 5 channels of data: 2 for the horizontal and vertical heatmaps, and 3 for the RGB image – all this data describes the same moment in time from two different perspectives. A supervision label  $y_i$ , containing, the “ground truth” values for each of the 15 keypoints, will be generated with the evaluation of  $\mathcal{M}_2(x_i[\text{RGB}])$ . Then, the training pair  $(x_i[\text{RF}], y_i)$  will be inputted into  $\mathcal{M}_1$ , resulting in final prediction vector  $\hat{y}_i$ . Loss will be computed as  $J(\theta, y_i, \hat{y}_i)$ , where  $J$  may represent a loss function (e.g. multiclass cross-entropy)

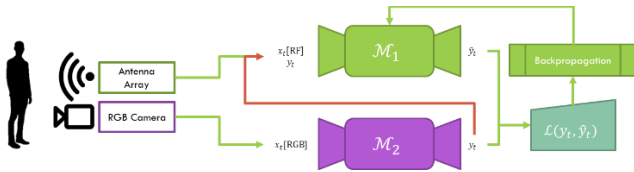


Figure 19. Cross-Modal Supervision

### C. Novel Training Pipeline with Artificial Obstruction

A supplemental stand is used to introduce RF obstruction without blocking the RGB camera: Wood, brick, drywall, concrete, plastic, paper board, insulation, linoleum, carpet, fog, leaves. This increases robustness of trained model through explicit learning on through-obstruction scenes.

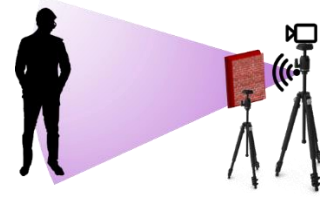


Figure 20. Training Setup

### D. Multilayer Perceptron (MLP) & Deep Neural Network

Deep Learning Neural Networks [22] are composed of layers of neurons, much like the biological brain. Each neuron takes in two values:  $p$ , the input, and  $p$ , the bias. Each neuron outputs one value:  $a = wp + b$ .  $a$  is then subject to an activation function  $\sigma(\cdot)$ , such as hyperbolic tangent or the rectified linear unit, that regularizes its value and introduces non-linearity; this produces final output  $a'$ .  $w$  and  $b$  are values that can be adjusted through training of the network to optimize results. Figure 21 diagrams the structure of a general neuron.

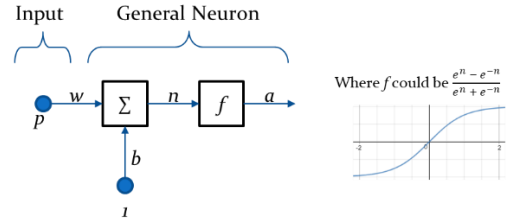


Figure 21. Structure of a General Neuron

Neurons can have many inputs, in the form of vectors. In this case, if  $\mathbf{p}$  is a vector of inputs,  $\ell$  is a layer of neurons, and  $\mathbf{W}$  is a weight matrix representing all connections between  $\mathbf{p}$  and  $\ell$ , and  $\mathbf{b}$  is a vector of bias values for each output, then the operations of a neuron are best represented by matrix multiplication. Output vector  $\mathbf{a}' = \sigma(\mathbf{W}\mathbf{p} + \mathbf{b})$ .

### E. Residual Convolutional Neural Network

In contrast to deep multilayer perceptron models where each layer is fully connected to the layers around it, each neuron in a vanilla Convolutional Neural Network (CNN) [17] is only locally connected with a few neurons in the surrounding layers. Additionally, all neurons in a CNN layer share identical weights. Mathematically, the value of a neuron in a CNN can be computed as the convolution of a weight kernel with the neurons in the previous layer:

$$a_n = \sigma(k_n * a_{n-1}) \quad (10)$$

where  $*$  is the convolution operator, and  $k_n$  is the weight kernel at layer  $n$ . CNNs leverage local dependencies and features in data – especially that of images – to reduce the total number of learned parameters. This acts as a regularization and resource reduction mechanism.

The neurons, or weight kernels  $k_n \forall n$ , in a CNN are referred to as feature maps, as they can be viewed as features that correspond to different parts of the input. Deeper layers, or layers with a large  $n$ , will learn increasingly abstract and global properties of the image. [23]

A derivative of the CNN, the Residual Convolutional Neural Network (abbr. ResNet) [24], is employed to achieve several goals: 1) Serve a better fit to the data by enabling deeper stacking of layers, as ResNet is shown to guarantee performance  $\geq$  that of a vanilla CNN with fewer layers, 2) Provide capability to learn complex features without risk of overfitting or vanishing gradients, and 3) Smooth the topology of  $\mathcal{L}$  for a more favorable gradient descent landscape.

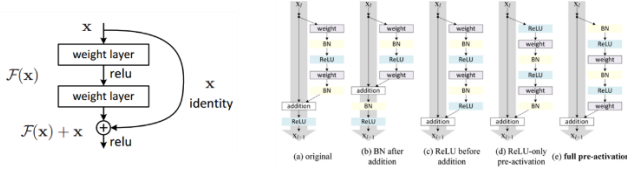


Figure 22. Residual CNN

#### F. Region Proposal Network to Decode Multiple People in Same Frame

A Region Proposal Network [25] is adopted to detect multiple people within a snapshot. The RPN detects objects by sliding a small network over the ResNet output feature map. RPN has two components: 1) Classifier: determines probability that object is contained within large sliding window, and 2) Regressor: given that classifier output is sufficiently high, refines coordinates of tight bounding box. The outputs of the RPN are cropped and outputted to the next deep learning module separately

#### G. Recurrent Neural Networks with Long Short-Term Memory (RNN-LSTM)

Recurrent Neural Networks (RNN) [16] are a variant of the traditional neural network. Instead of taking input only from the current time step in a sequence, they additionally take the input and output of previous time steps. Due to this, RNN's are optimal for analyzing data with temporal dependencies.

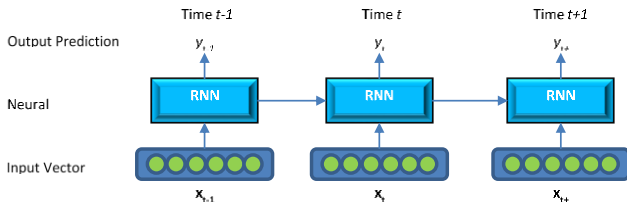


Figure 23. Unwrapped RNN for Visualization

However, basic RNN's are known to suffer from the vanishing and exploding gradient problem; when training gradients are passed through many time steps, they may exponentially increase or decay, resulting in the loss of long-term dependencies [26]. Long Short-Term Memory (LSTM) solves this problem by providing key modifications [27]. Namely, input, output, and forget gates are introduced to retain long term dependencies. Figure 19 diagrams the components of an RNN-LSTM cell.

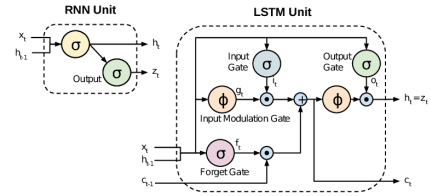


Figure 24. Comparison Between LSTM and RNN Cell

Because Recurrent Neural Networks are so effective at modelling temporal relationships, they are optimal for many-to-many imaging, as they accumulate RF information over time to recover a complete pose. This is in comparison to [35], which utilizes direct 3D convolutions to decode pose. However, 3D convolutions can aggregate less information due to the limitations to the kernel size [36].

#### H. Backpropagation Algorithm

Denote:  $y_t$  is the label at time  $t$  and  $\hat{y}_t$  is the prediction at time  $t$ ,  $\mathcal{L}$  is the objective function that is to be optimized via gradient descent,  $\theta$  defines the parameters of the neural network,  $\alpha$  is the selected learning rate constant and  $\gamma$  is the selected momentum constant.

The objective function can be given by Cross-Entropy Loss [28], which is expressed as:

$$\mathcal{L}(y, \hat{y}) = - \sum_t y_t \log \hat{y}_t \quad (11)$$

Backpropagation through time [29] is utilized to train the neural network, with Stochastic Gradient Descent (SGD) [30] as the optimizer and Cross-Entropy as an objective. SGD evaluates the training gradient on just one sample, as opposed to the entire training set, in order to reduce the computational complexity of neural network training. The standard update for each iteration is given by:

$$\theta = \theta - \alpha \nabla_{\theta} \mathcal{L}(\theta; y_t^{(i)}, \hat{y}_t^{(i)}) \quad (12)$$

However, it has been observed that vanilla SGD has two problems that are solvable by minor modifications to the training algorithm. Firstly, SGD has trouble dealing with certain objective function topologies and may converge slowly after steep initial gains. Therefore, momentum  $\gamma$  [31] is introduced to push the gradient in the direction of its travel, hence producing faster convergence. This is called SGD w/ Momentum (SGDM) and leads to the update:

$$\theta = \theta - \gamma v - \alpha \nabla_{\theta} \mathcal{L}(\theta; y_t^{(i)}, \hat{y}_t^{(i)}) \quad (13)$$

The second significant problem with SGDM is its tendency to be relatively erratic, as the gradients are computed with just one sample. To solve this problem, a variation is introduced, called Mini-Batch Gradient Descent w/ Momentum [32], which is also sometimes simply called SGDM with Mini-Batches. Instead of calculating the training gradients on one sample, several samples are chosen, and their partial derivatives are averaged. With this, the final training update is given by:

$$\theta = \theta - \gamma v - \alpha \frac{1}{b} \sum_{i=k}^{k+b} \nabla_{\theta} \mathcal{L}(\theta; y_t^{(i)}, \hat{y}_t^{(i)}) \quad (14)$$



Below is an example of gradient descent navigating the topology of a certain cost function using a model with parameters  $\theta_0$  and  $\theta_1$  (linear regression can be considered an example of this). As it is evident, the parameters are initialized to an arbitrary value, after which they are repeatedly tuned until the application of those parameters yields a local minimum in loss.

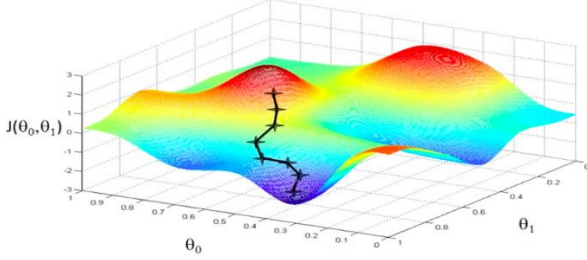


Figure 25. Visualization of Gradient Descent Traversing Cost Function Topology

#### I. Novel Objective Function to Reduce Overfitting

With a high number of output neurons ( $48 \times 64 \times 15 = 46080$  per timestep), overfitting is a considerable risk. To combat this, a novel objective function is proposed by the researcher:

$$\mathcal{L} = \sum_t \sum_p \sum_k \sum_i C_{pk} e^{-\left(\log 2 - \delta(y_{pki}, \hat{y}_{pki})\right)} y_{pki} \log \hat{y}_{pki} \quad (15)$$

where  $T$  is #timesteps,  $P$  is #people,  $K$  is #keypoints,  $C$  is #classes, and  $\delta(y_{ki}, \hat{y}_{ki})$  represents the pixel distance between the predicted and ground-truth outputs.  $\mathcal{L}$  penalizes the model highly for misclassifying keypoints far from the ground truth and less so for closer mistakes (on an exponential scale).  $\mathcal{L}$  also considers the confidence output of the cross-modal supervisory model  $C_k$  for each keypoint  $k$ , making penalties more severe if the label confidence is higher.

#### J. Original Researcher-Created Dataset Containing Adversarial Examples

5000 training samples of {RF, RGB} images were collected at multiple locations. Multiple mediums were also traversed: wood, brick, drywall, plastic, paper board, and open air were selected for testing. Data was partitioned 65/5/30 for training/validation/testing, respectively.

Table 4. Dataset Details

	No Person	Walking	Gesturing	Sitting	Multi-Person	Total
Visible Scene	250	1250	750	250	500	3000
Occluded Scene	250	750	500	250	250	2000
Total	500	2000	1250	500	750	5000

The no-person scenes can be considered as adversarial examples. These are designed to fool the neural network – they may contain RF signatures that could be mistaken for humans but are not. Training the deep learning model on these examples prevents the case in which there is no person, but the neural network detects phantom ones in the scene. Due to time considerations in completing this project, 5 subjects were used.

#### K. Model Summary

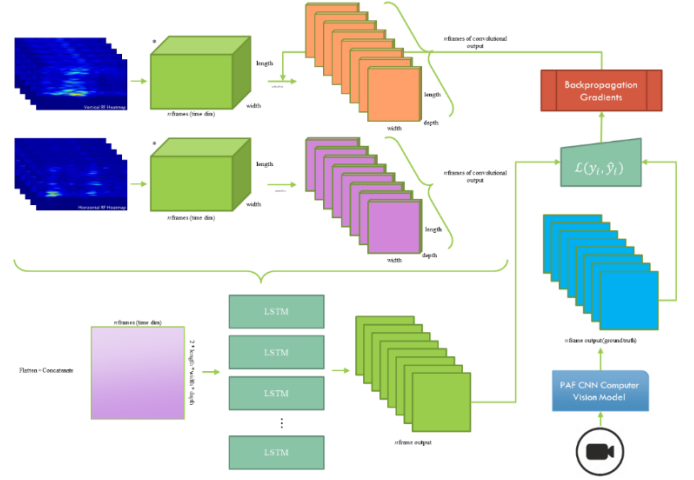


Figure 26. Summary

#### L. Pseudocode for Training and Testing and Prediction

Shown below is pseudocode for the training process.

```

Input sequences
Split into Mini-Batches
FOR all Mini-Batches
  FOR each sequence in Mini-Batch:
    FOR each time step in current sequence:
      Predict class of action
      Compare prediction to ground truth y_t
      Calculate loss
      Add to accumulating loss
    ENDFOR
  ENDFOR
  Apply changes to weights based on accumulated loss
ENDFOR

```

Testing evaluates performance on new data the neural network did not see during training. Results are analyzed with the methods in §XI. Shown below is the pseudocode for the testing process.

```

FOR each sequence in input:
  FOR each time step in current sequence:
    Calculate confidence that each class is correct
    Determine class with highest confidence (argmax)
    Record predictions and result
  ENDFOR
  Store predictions over all time steps
ENDFOR
Analyze

```

### XI. OUTPUT AND PERFORMANCE ANALYSIS

Feature analyses, performance analyses, cost analyses, and testing results all show this project to be legitimate and robust.

#### A. Feature and Performance Analysis

Features were compared with status quo solutions to visible sight being obstructed by walls, debris, or other miscellaneous functions:

Table 4. Feature Analysis

Feature	Without Project	With Project	Improved?
Visual Perception in Free Air	Visible Light	Radio Frequency	n/a
Visual Perception Behind Wall	Impossible	Detection of approximate body form	✓
Fire Emergency	Visible light & IR are unable to penetrate smoke & fire	RF signals can penetrate obstruction	✓★
Search and Rescue	Heart rate detector used Susceptible to seismic noise	Precise detection of location and pose of body	✓
Senior Healthcare	Invasive: requires wearing of restrictive sensors	Noninvasive monitoring	✓
Military Breach	Deadly risk for soldiers: building occupants unknown	Precise detection of hostiles	✓

### B. Training Plot Analysis

Accuracy represents how well the neural network performs on training data. 100% training accuracy indicates convergence, which means the selected model is appropriate. Loss represents neural network's aggregated error at each time step. Low, non-zero loss indicates a good fit, as opposed to overfitting and underfitting. [33]

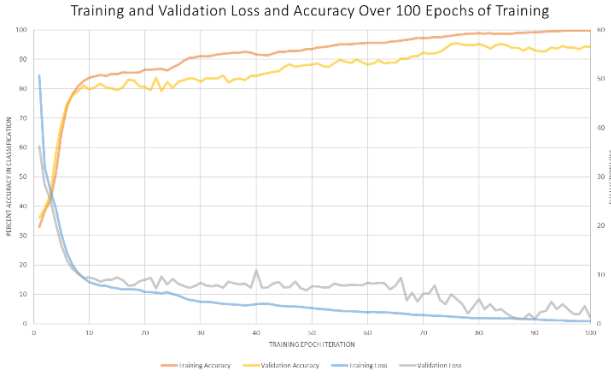


Figure 27. Accuracy and Loss Plot for Training

### C. OKS Analysis

The Object Keypoint Similarity (OKS) [34] metric quantifies the average quality of keypoint localization over all 15 bodily keypoints defined in BODY\_15. Keypoint Similarity (KS) is computed by evaluating an un-normalized Gaussian distribution. Where  $\hat{\theta}^{(p)}$  are classified keypoints of person  $p$ ,  $\theta^{(p)}$  are ground truth locations,  $C_i$  is the prediction's confidence level, and  $s$  and  $k_i$  are constants used to scale  $\sigma$  of the distribution:

$$\left\{ \begin{aligned} OKS(\hat{\theta}^{(p)}, \theta^{(p)}) &= \frac{\sum_i KS(\hat{\theta}_i^{(p)}, \theta_i^{(p)}) \delta(C_i > 0)}{\sum_i \delta(C_i > 0)} \\ KS(\hat{\theta}_i^{(p)}, \theta_i^{(p)}) &= e^{-\frac{\|\hat{\theta}_i^{(p)} - \theta_i^{(p)}\|_2^2}{2s^2k_i^2}} \end{aligned} \right. \quad (16)$$

Average Accuracy  $AA_{KS}^{(p)}$  of classification for each person can be computed at various KS values: Given a threshold  $T_{KS}$ , compute the proportion of keypoints on person  $p$  that fulfill  $KS \geq T_{KS}$ .  $AA$  can also be computed per keypoint over the entire dataset. For context, ~95% of human-annotated keypoints will have  $KS \geq .75$ . As such,  $KS = .75$  is considered a highly strict match;  $KS = .50$  is a medium match.

#### i. Individual Keypoint Classification Error

General trends are analyzed for KS values of all keypoint types. The majority of keypoints are classified with low-to-none error. Only 6% of keypoints are collected with High Error or worse. Shoulder and Hips are classified with highest consistency and accuracy. Hands and Feet are most difficult to classify.

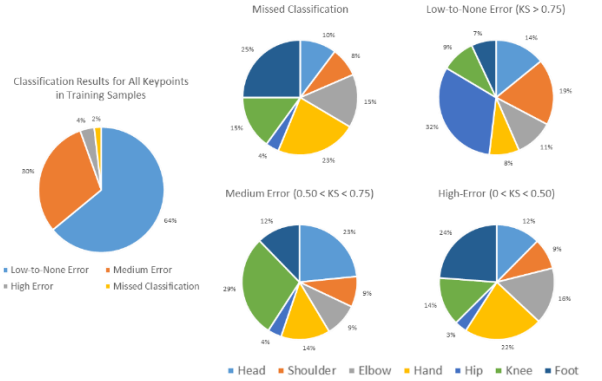


Figure 28. KS Performance by Keypoint

#### ii. Individual Keypoint AA on Various KS Levels & Obstruction Statuses

Putting the individual keypoint analyses together, AA for each keypoint is calculated at 2 differing threshold values:  $KS_{50}$ , and  $KS_{75}$  (loose fit vs. strict fit). Data collected on both visible and through-obstruction scenes. Keypoints can be classified with high accuracy even at strict fit.

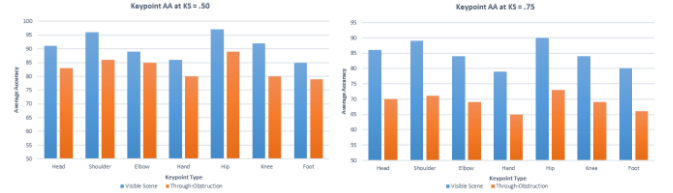


Figure 29. Keypoint AA at Various KS

#### iii. OKS Comparison with State-of-the-Art RGB Vision

AA for RF pose parsing on visual scenes is compared to the reported values for OpenPose, a state-of-the-art RGB image pose-decoding software. AA for RF pose parsing on through-obstruction scenes is measured.

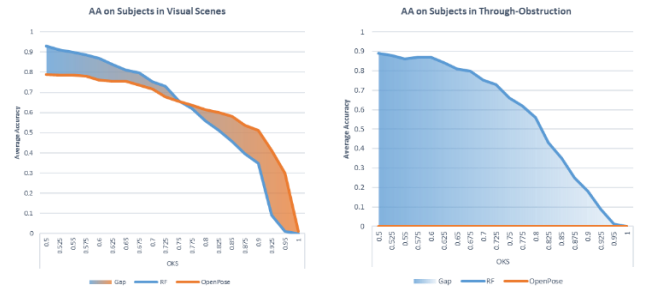


Figure 30. AA Over Multiple OKS

RF outperforms OpenPose on low-threshold classification. Possible reasons include that the novel objective function (eq. 13) reduces overfitting, and that we employ many-to-many imaging using LSTM RNN's (§IX-G) to consider multiple

frames of input; this contrasts with the frame-by-frame processing approach for OpenPose.

RF has high performance even for through-obstruction inference. Possible reasons include the novel training pipeline introduced in §X-B and the many-to-many imaging technique detailed in §X-G.

#### iv. Medium Analysis

The following graph compares AA through different types of obstruction. Typical types of obstruction have minimal impact on performance depending on their dielectric constant.

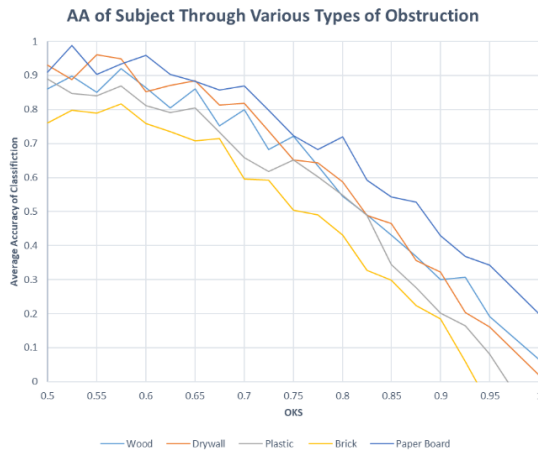


Figure 31. Medium Analysis

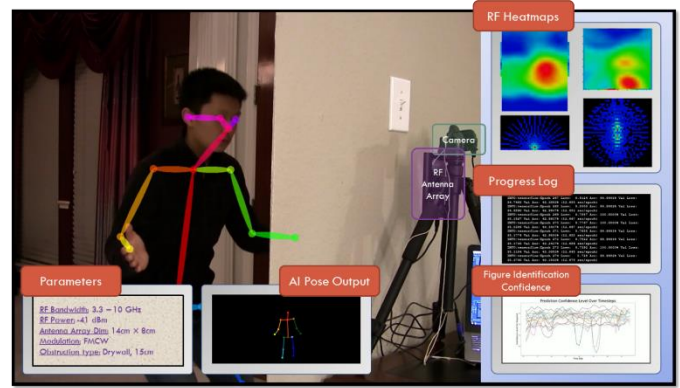
## XII. CONCLUSION

This project establishes a novel breakthrough artificial intelligence imaging methodology that can recover human figures behind obstruction. Analogous to the visible light that powers our vision, FMCW-Modulated Microwave Radio-Frequency signals transmitted from an antenna array are used to “illuminate” humans behind obstruction. The key contribution is the proposal of a many-to-many imaging methodology, in contrast to one-to-one imaging for optical systems. This overcomes the specular reflection limitation using latest AI technological developments to synthesize time-sequential data. One particularly notable application of this work is the detection of people trapped in burning buildings or foliage of the forest from safety.

Contributions are summarized as follows: 1) Created a many-to-many imaging decoder using RNN-LSTM. 2) Proposed a novel objective function for anti-overfitting optimization. 3) Employed Residual CNN model for learning highly robust features. 4) Adopted Region Proposal Network for multi-person detection in the same frame. 5) Implemented a new training pipeline to solve a bottleneck with non-explicit training. 6) Created a simulator in a non-trivial effort to show system usability. 7) Wrote 4,000+ lines of code in implementation. 8) Curated an original 30GB dataset that used adversarial examples to improve robustness. 9) Plan to release code & dataset to the open-source community.

If applied to the global population, this technology could help millions in need and save thousands of lives each year.

## XIII. DEMO SIMULATOR



## XIV. REFERENCES

- [1] <https://www.usfa.fema.gov/data/statistics/>
- [2] P. Wang et al. FMCW Radar Imaging with Multi-channel Antenna Array via Sparse Recovery Technique. 2010.
- [3] P. L. Ryan. Radio Frequency Propagation Differences Through Various Transmissive Materials. Univ. of North Texas, 2017.
- [4] M. A. Richards. Fundamentals of Radar Signal Processing (Second ed.). Published by McGraw Hill, 2014.
- [5] Antenna Patterns and Their Meaning. <https://goo.gl/pQExs3>. Corporate-published by Cisco (n.d.)
- [6] S. J. Orfanidis. Electromagnetic waves and antennas. Rutgers University, 2002.
- [7] F. Adib. Capturing the Human Figure Through a Wall. In ACM TOG, 2015.
- [8] H. El et. al. Sub-nanosecond Time Synchronization Mechanism for Radio Interferometer Array. 2017.
- [9] C. Nickolas The Basics of Mixers. <https://goo.gl/B7uut5>
- [10] Mahafza, B. R. 2013. Radar systems analysis and design using MATLAB. Chapman & Hall.
- [11] C. M. Dissanayake et al. Signal Propagation Effects of Radio Link in Fire Environments. In IEEE, 2010.
- [12] <https://api.walabot.com/>
- [13] Spherical Coordinates. <https://goo.gl/nAFPMF> (Lamar Math Tutorials Site)
- [14] Cook. The Laws of Reflection and Refraction. University of Georgia, 2015.
- [15] F. R. Hallett. Dynamic light scattering. In Food Research International Vol. 27, 1994.
- [16] M. I. Jordan. Attractor dynamics and parallelism in a connectionist sequential machine. In Cognitive Science Conference 1986.
- [17] Krizhevsky et al. Deep Convolutional Neural Networks. Commun. In ACM Transactions, 2012.
- [18] J. Goodfellow et al. Generative Adversarial Nets. In NIPS, 2014.
- [19] S. Zhao et al. InfoVAE: Information Maximizing Variational Autoencoders. In CoRR, 2017.
- [20] Z. Cao et al. OpenPose: Realtime Multi-Person 2D Pose Estimation using Part Affinity Fields. In CVPR, 2017.
- [21] Evaluating Machine Learning Methods. University of Wisconsin-Madison.
- [22] F. Murtagh. Multilayer perceptrons for classification and regression. In Neurocomputing, 1991.
- [23] R. Mopuri, U. Garg. An unraveling approach to visualize the discriminative image regions. arXiv 1708.06670.
- [24] He, et al. Deep Residual Learning for Image Recognition. In CVPR and arXiv 1512.03385.
- [25] S. Ren, K. He, et al. Faster R-CNN: Towards Real-Time Object Detection with Region Proposal Networks. In NIPS 2015.

- [26] Pascanu, Razvan & Mikolov, Tomas & Bengio, Y. On the difficulty of training Recurrent Neural Networks. In ICML, 2013.
- [27] S. Hochreiter and J. Schmidhuber. Long short-term memory. In Neural computation, 1997.
- [28] Janocha et al. On Loss Functions for Deep Neural Networks in Classification. arXiv 1702.05659, 2017.
- [29] P. J. Werbos. Backpropagation through time: what it does and how to do it. In Proceedings of the IEEE, 1990.
- [30] Kiefer, Joe & Wolfowitz, J. Stochastic Estimation of the Maximum of a Regression Function. In AMS, 1952.
- [31] Loizou et al. Momentum and Stochastic Momentum for Gradient Descent Methods. The University of Edinburgh, 2017.
- [32] M Li, T. Zhang, et al. Efficient Mini-batch Training for Stochastic Optimization. In KDD, 2014.
- [33] Nitish Srivastava et al. Dropout: A Simple Way to Prevent Neural Networks from Overfitting. In JMLR, 2014.
- [34] M. Ronchi et al. Benchmarking and Error Diagnosis in Multi-Instance Pose Estimation. arXiv 1707.05388v2
- [35] M. Zhao et al. Through-Wall Human Pose Estimation Using Radio Signals. In CVPR, 2018.
- [36] Z. Zuo et al. Convolutional recurrent neural networks: Learning spatial dependencies for image representation. In CVPRW, 2015.
- [37] <https://www.xsens.com/>
- [38] M. Kok et al. Using Inertial Sensors for Position and Orientation Estimation. In arXiv:1704.06053.
- [39] J. Xiong et al. Arraytrack: A fine-grained indoor location system. In Proceedings of the USENIX NSDI, 2013.
- [40] M. Kotaru et al. Spotfi: Decimeter level localization using wifi. In ACM SIGCOMM Computer Communication Review, 2015.
- [41] F. Adib et al. 3D tracking via body radio reflections. In Proceedings of the USENIX NSDI, 2014.
- [42] W. Wang et al. Gait recognition using WiFi signals. In Proceedings of the ACM UbiComp, 2016.
- [43] P. Melgarejo et al. Leveraging directional antenna capabilities for fine-grained gesture recognition. In Proceedings of the ACM UbiComp, 2014.